ACS APPLIED MATERIALS & INTERFACES

Research Article

www.acsami.org

Solvents Induced ZnO Nanoparticles Aggregation Associated with Their Interfacial Effect on Organic Solar Cells

Pandeng Li,[†,‡] Tonggang Jiu,*[,†] Gang Tang,[†] Guojie Wang,[†] Jun Li,[†] Xiaofang Li,[‡] and Junfeng Fang*[,†]

[†]Institute of New Energy Technology, Ningbo Institute of Material Technology and Engineering (NIMTE), Chinese Academy of Science (CAS), Ningbo, Zhejiang 315201, People's Republic of China

[‡]School of Chemistry and Chemical Engineering, Hunan University of Science and Technology, Xiangtan, Hunan 411201, People's Republic of China

Supporting Information

ABSTRACT: ZnO nanofilm as a cathode buffer layer has surface defects due to the aggregations of ZnO nanoparticles, leading to poor device performance of organic solar cells. In this paper, we report the ZnO nanoparticles aggregations in solution can be controlled by adjusting the solvents ratios (chloroform vs methanol). These aggregations could influence the morphology of ZnO film. Therefore, compact and homogeneous ZnO film can be obtained to help achieve a preferable power conversion efficiency of 8.54% in inverted organic solar cells. This improvement is attributed to the decreased leakage current and the increased electron-collecting efficiency as well as the improved interface contact with the active layer. In addition, we find the enhanced maximum exciton generation rate and exciton dissociation probability lead to the improvement of device performance due to the preferable ZnO dispersion. Compared to other methods of ZnO nanofilm fabrication, it is the more convenient, moderate, and effective to get a preferable ZnO buffer layer for high-efficiency organic solar cells.

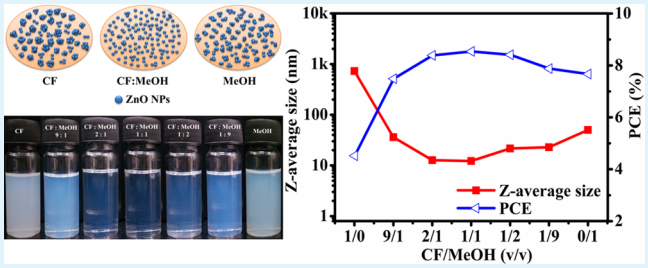

KEYWORDS: *aggregations of ZnO nanoparticles, mixed solvents, cathode buffer layer, inverted organic solar cells*

1. INTRODUCTION

Organic solar cells (OSCs) have been receiving considerable attention in recent years due to their advantages such as low-cost, flexibility and lightweight.[1−3] In the past few years, a remarkable improvement in the power conversion efficiencies (PCEs) up to 10% has been achieved.[4−8] However, the acidic nature of poly(3,4-ethylenedioxythiophene):poly-(styrenesulfonate) (PEDOT:PSS) used as a hole-transport layer in forward OSCs always corrodes the indium tin oxide (ITO) anode, together with the easy oxidization of low-work-function metal cathode, resulting in degradation of the device.[9−12] One approach to alleviate the problems is to use inverted device architecture. In the inverted structure, the *n*-type metal oxides (ZnO, TiO_x) prepared by different methods are employed as the cathode buffer layer between ITO and the active layer.[13,14] The inorganic materials present apparent surface defects, leading to poor interfacial contact with the active layer and severe back charge recombination.[15,16] Thus, enormous efforts have been dedicated to the interfacial modification and fabrication for improving electron-collecting efficiency.

Different methods have been applied to fabricate an *n*-type metal oxides (ZnO, TiO_2, TiO_x) buffer layer, such as doping metals nanoparticles to *n*-type metal oxides films,[17−19] adding the polymers or organic small molecules on the *n*-type metal oxides to prepare bilayer film,[20,21] organic−inorganic hybrid film,[22−30] and inorganic *n*-type metal oxides hybrid film.[31,32] Moreover, the sol−gel method of metal oxides with block copolymer assist also provides various structural films for organic photovoltaic devices.[33−36] By the means, in addition to fill the surface defects of *n*-type metal oxide films, they help improve the charge carrier mobility and interfacial contact with the active layer. However, the above methods of interface modification increase process steps or introduce more operating parameters, which are not beneficial to large-scale preparation and industrialization of devices. So, the simple and convenient methods based on sole *n*-type metal oxides should be exploited.

In the studies of pursuing high performance photovoltaic devices, the solvent effect has been found to optimize the morphology of active layer, which results in the improvement of exciton dissociation efficiency and transportation efficiency of charge carrier in the active layer.[37−39] However, few studies have been done to improve the morphology of the *n*-type metal oxides based cathode buffer layer.

In this study, we found that the aggregations of ZnO nanoparticles (NPs) could be controlled by simply adjusting the volume ratio of binary solvents (chloroform (CF) vs

Received: August 3, 2014
Accepted: September 30, 2014
Published: September 30, 2014

 © 2014 American Chemical Society

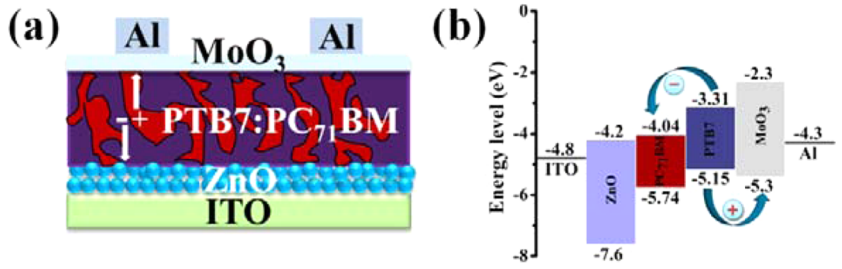

Figure 1. (a) Device architecture of the inverted OSCs with ZnO film as cathode buffer layer; (b) energy level diagram of the various device components.

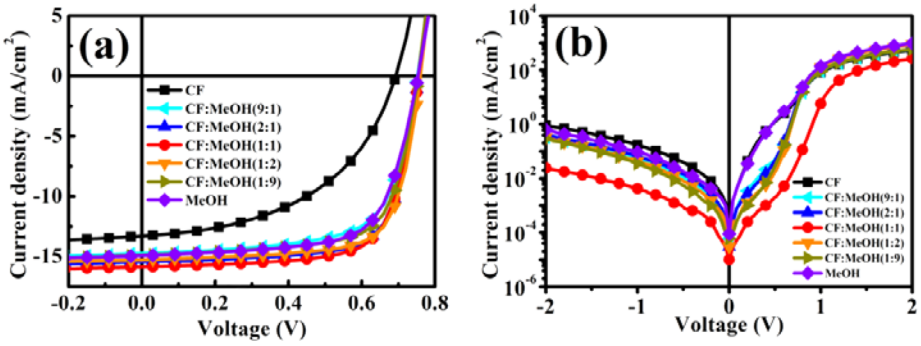

Figure 2. (a) Illuminated and (b) dark $J-V$ characteristics of ITO/ZnO/PTB7:$PC_{71}BM$/MoO_3/Al architecture with buffer layers deposited from the ZnO NPs solution with different ratios mixture of binary solvents.

methanol (MeOH)). This method supports a simple but effective way to fabricate the favorable buffer layer in photoelectric devices including organic solar cells. In this way, the morphology of ZnO film is highly relevant to the solution aggregations, and controllable. Therefore, the compact and homogeneous ZnO nanofilm is obtained to support a PCE of 8.54% by interfacial modification of inverted OSCs with open-circuit voltage (V_{oc}) of 0.756 V, a short-circuit current (J_{sc}) of 15.85 mA/cm^2, and a fill factor (FF) of 71.3%, under AM 1.5G 100 mW·cm^{-2} simulated solar light. The device performance is much better than those based on the sole ZnO buffer layer before optimization. The effects of solvent ratios on the solution properties, film morphology and the device parameters as well as exciton generation and dissociation rate are discussed in details.

2. EXPERIMENTAL SECTION

Materials and Characterization. Indium tin oxide (ITO)-coated glass substrates were purchased from CSG HOLDING Co., LTD (China) ($R_s \leq 10\ \Omega/\square$ $T_r \geq 83\%$). Electron-donor material PTB7 and electron-acceptor material $PC_{71}BM$ were purchased from 1-material Chemscitech and Nano-C, respectively. MoO_3 was obtained from Alfa Aesar. Chlorobenzene and 1,8-diiodoctane were provided by Sigma-Aldrich. The zinc acetate dihydrate ($Zn(Ac)_2{\cdot}2H_2O$), potassium hydroxide (KOH), methanol, and chloroform were bought from Sinopharm Chemical Reagent Co. and used as received.

The current−voltage ($J-V$) characterization was taken using a Keithley 2400 source measure unit under AM 1.5G simulated solar light. The external quantum efficiency (EQE) was performed by the IQE200TM data acquisition system. The particle size and distribution of samples were analyzed using dynamic light scattering equipment (Zetasizer Nano ZS, Malvern, U.K.). Surface morphology and film roughness of the specimens were obtained using scanning electron microscopy (SEM) (S-4800) operated at an acceleration voltage of 4 kV and atomic force microscopy (AFM). AFM measurements were operated in tapping mode using a Veeco dimension V atomic microscope. Film thickness measurement was carried on profile meter (Dektak150).

Preparation of the ZnO NPs solution. ZnO nanoparticles were prepared according to the procedures.[40,41] The mixed solvents with different ratios are used to dissolve the nanoparticles to obtain a sol with, on average, 15 mg·mL^{-1} ZnO solutions.

Device Fabrication and Characterization. The devices were fabricated on ITO-coated glass substrates and the ITO-coated glasses were cleaned by a sequence of detergent, deionized water, acetone, and isopropyl alcohol for 15 min inside an ultrasonic bath, dried with nitrogen stream, and subsequently treated with UV-ozone for 30 min. The obtained ZnO solutions were spin-coated onto the precleaned ITO substrates at 1500 rpm (about 65 nm) and then were annealed at 80 °C for 10 min. The chlorobenzene blend solution (3 vol % 1,8-diiodoctane) of PTB7:$PC_{71}BM$ (10:15 mg·mL^{-1}) was then spin-coated at 2000 rpm for 120 s on top of the ZnO nanofilm. Finally, device fabrication was achieved by thermal evaporation of 10 nm of MoO_3 and 100 nm of Al as the anode under the vacuum of about 1×10^{-6} mbar, and the device area was 0.04 cm^2.

3. RESULTS AND DISCUSSION

Figure 1a presents the structure of the inverted OSCs used in this study: ITO/ZnO nanofilm/active blends/MoO_3/Al. The ZnO cathode buffer layer is deposited from the solution of ZnO NPs dispersed in co-solvent mixture (CF and MeOH). The active layer is composed of the blend of poly[[4,8-bis[(2-ethylhexyl)oxy]benzo[1,2-*b*:4,5-b′]dithiophene-2,6-diyl][3-fluoro-2-[(2-ethylhexyl)carbonyl]thieno[3,4-*b*]thiophenediyl]] (PTB7) as the electron donor and (6,6)-phenyl C71-butyric acid methyl ester ($PC_{71}BM$) as the electron acceptor. To get the energy level alignment of various device components, the cyclic voltammetry (CV) was carried out to investigate the electrochemical properties of $PC_{71}BM$.[42] The energy levels of ZnO NPs were determined by ultraviolet photoelectron spectroscopy (UPS) and the UV absorption edge.[31] The electronic energy levels of PTB7 and MoO_3 were taken from the literatures.[43,44] Consequently, the energy level diagram of

Table 1. Summary of the Photovoltaic Parameters of PTB7:$PC_{71}BM$ Devices Using Buffer Layers Deposited from ZnO NPs Solution with Different CF/MeOH Volume Ratios[a]

solvents ratios (CF: MeOH)	V_{oc} (V)	J_{sc} (mA/cm^2)	FF (%)	PCE (%) best/average[b]	R_s (Ω·cm^2)	R_p (kΩ·cm^2)	RR (10^3dark)
1:0	0.693	13.27	49.1	4.52/3.74	9.04	0.40	0.60
9:1	0.752	14.74	67.6	7.49/7.28	4.76	0.83	1.82
2:1	0.754	15.44	72.1	8.39/8.10	4.00	1.17	2.37
1:1	0.756	15.85	71.3	8.54/8.46	4.36	1.26	11.2
1:2	0.759	15.26	72.6	8.41/8.26	3.92	1.15	2.72
1:9	0.754	14.88	70.2	7.88/7.73	4.24	0.85	2.03
0:1	0.753	14.91	68.3	7.67/7.45	5.76	0.87	1.56

[a]The rectification ratio (RR, defined as the ratio of forward-to-reverse bias current density at a bias voltage of ±2 V) was obtained from dark $J-V$ characteristics. The R_s and the R_p are the series resistance and the shunt resistance of PTB7:$PC_{71}BM$ devices, respectively. [b]The average PCE values are averaged by eight devices. The device parameter distribution maps are presented in Figure S1 in the Supporting Information.

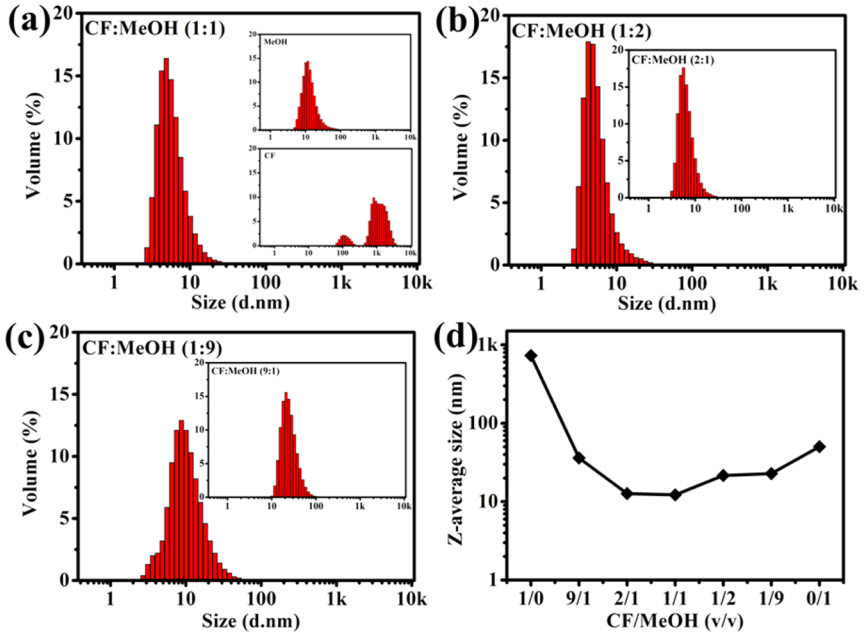

Figure 3. Particle-size distributions of ZnO NPs dispersed in mixed solvents with different volume ratios (CF and MeOH). (a) pure CF, pure MeOH, and 1:1 (v/v); (b) 1:2 (v/v), 2:1 (v/v); (c) 1:9 (v/v), 9:1 (v/v); (d) Z-average size of ZnO NPs.

various device components is shown in Figure 1b. It is clear that the conduction band (CB) of ZnO (−4.2 eV) is slightly lower than the lowest unoccupied molecular orbital (LUMO) of $PC_{71}BM$ (−4.04 eV), which builds the preferable energy level cascade to facilitate electron transfer from $PC_{71}BM$ to the ITO electrode. In addition, the ZnO nanofilm can prohibit the hole transport from PTB7 to the ITO electrode because the valence band (VB) of ZnO (−7.6 eV) is lower than those of PTB7 (−5.15 eV) and $PC_{71}BM$ (−5.74 eV). Therefore, from the viewpoint of energy levels, the ZnO nanofilm is beneficial for electron collection and diminishing carrier recombination. Moreover, the LUMO (−2.3 eV) of MoO_3 inhibits the electron transport from $PC_{71}BM$ to the Al electrode. Meanwhile, the VB (−5.3 eV) of MoO_3 is close to the HOMO of PTB7 (−5.15 eV). According to the previous reports,[45,46] the MoO_3/polymer Fermi level alignment likely equilibrate to ≈0.3 eV above the HOMO level. Thus, the holes can be efficiently transported to Al electrode through MoO_3 without obvious energy loss.

Figure 2a displays the illuminated current−voltage ($J-V$) characteristics of PTB7:$PC_{71}BM$ devices using ZnO buffer layers. Table 1 summarizes the detailed device parameters. It can be observed that the device based on ZnO NPs dispersed in pure CF exhibits the lowest PCE of 4.52%. With the volume ratio changing from 9:1 to 2:1, the V_{oc}, J_{sc}, and FF of devices increase gradually, so the PCEs increase from 7.49% to 8.39%. When the volume ratio reaches 1:1, the device achieves a V_{oc} of 0.756 V, a J_{sc} of 15.8 mA/cm^2, and a FF of 71.3%, giving the highest PCE of 8.54%. However, when the volume ratios are under 1:1 and eventually change into pure MeOH, it leads to decreased J_{sc} and FF. The V_{oc} remains almost unchanged. Consequently, the PCE decreases from 8.54% to 7.67%. So, the optimized volume ratio of binary solvents is 1:1, which gives the best average PCE of 8.46%. The influence of solvents ratios to the device performance should be investigated in more depth.

Figure S2 (Supporting Information) clearly presents different aggregations depending on solvents ratios. The ZnO solution in the 1:1 volume ratio displays a transparent solution. In contrast, the solution with the high ratio is cloudy, implying the formation of ZnO NPs aggregation. To probe the relationship between the aggregation of ZnO NPs and the mixed volume ratios, Zetasizer Nano ZS equipment is applied to measure the particle size distributions (by volume) and the results are revealed in Figure 3.[47] Under the pure CF condition, the severe aggregation is clearly shown due to strong net attraction among

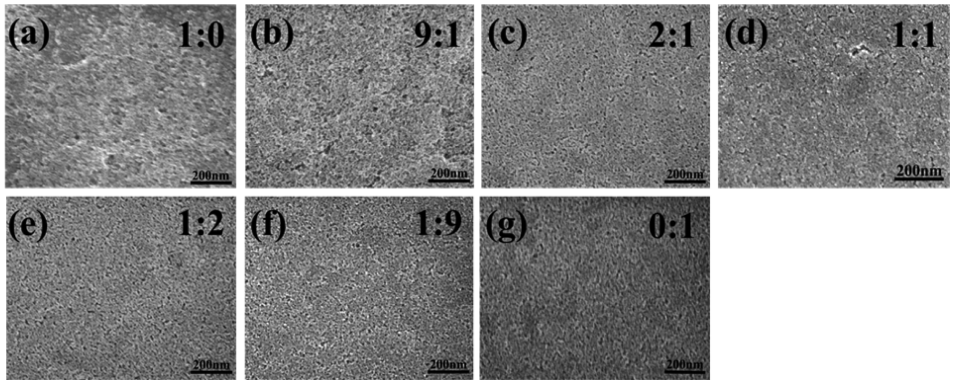

Figure 4. SEM images of ZnO buffer layers derived from ZnO NPs solutions with different solvent volume ratios (CF:MeOH), (a) 1:0 (pure CF), (b) 9:1, (c) 2:1, (d) 1:1, (e) 1:2, (f) 1:9, (g) 0:1 (pure MeOH).

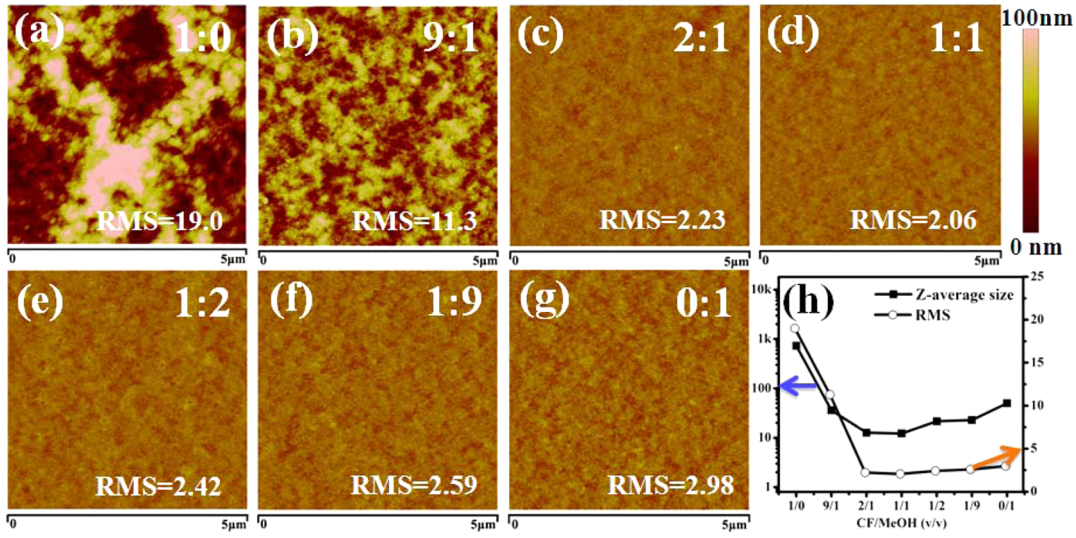

Figure 5. AFM images of ZnO buffer layers derived from ZnO NPs solutions with different CF/MeOH ratios (v/v), (a) 1:0 (pure CF), (b) 9:1, (c) 2:1, (d) 1:1, (e) 1:2, (f) 1:9, (g) 0:1 (pure MeOH). (h) Comparative analysis images between aggregation variation of ZnO NPs and RMS roughness variation of ZnO nanofilm.

small ZnO NPs. And yet the aggregation is obviously reduced at the condition of 9:1 (CF:MeOH (v/v)). This indicates that the aggregation of ZnO NPs is very sensitive to the relative concentration of MeOH.

Because the dispersion of NPs is usually dominated by interaction between the surface ligands and the solvents, the hydroxyl groups of MeOH here covering the surface of ZnO NPs are expected to contribute to dispersion in such solvents system. Then, the relative energy difference provides evaluation of dispersibility of the ZnO NPs in various solvents such as CF and MeOH in this work. Here, adding MeOH to CF improves the dispersion of ZnO NPs, as shown from the transparency change of colloidal ZnO solution presented in Figure S2 (Supporting Information) by changing the relative energy difference due to modification of hydrogen bonding interaction in solvents.[48] When the appropriate mixing volume ratios (2:1, 1:1, 1:2) are prepared, the preferable size distributions of ZnO NPs are obtained. However, the size distributions shift toward larger size ranges again with further increase of the MeOH ratio. To further study the aggregation variations of ZnO NPs, the *Z*-average size of ZnO NPs that increases as the particle size increases is as a function of solvents ratios of ZnO NPs solution. The result, presented in Figure 3d, is in good agreement with that of particles-size analysis. Meanwhile, the optimized volume ratio of binary solvents is concluded as 1:1, in which the smallest *Z*-average size is achieved, indicating that the ZnO NPs possess the best dispersion in the mixed solvents system and the dispersity of ZnO NPs is affected by the molecular interactions from polar solvents.[48]

To figure out the effect of aggregation variation on the surface morphology of ZnO nanofilm, the SEM and AFM are employed to investigate the surface morphology of ZnO nanofilm.[49] As shown in Figures 4 and 5, the root-mean-square (RMS) roughness value of ZnO nanofilm made from the pure CF condition is 19.0 nm. The increased pore size and the aggregation of ZnO NPs can be apparently found in the film, indicating that the film is an uncontinuous film with large roughness. When the MeOH is added and the mixed volume ratios are changed into 9:1 and 2:1, the RMS roughness and the void size of ZnO nanofilms decrease dramatically and the dense films were formed. With the solvents ratios changed to 1:1, the ZnO nanofilm is smoothest with a lowest RMS roughness of 2.06 nm. Thus, the dense and homogeneous ZnO nanofilm is obtained. However, further change of solvent ratios to 1:2, 1:9, and pure MeOH results in increased roughness and void size. As a result, the RMS variations from AFM measurements are

dx.doi.org/10.1021/am5051789 | *ACS Appl. Mater. Interfaces* 2014, 6, 18172−18179

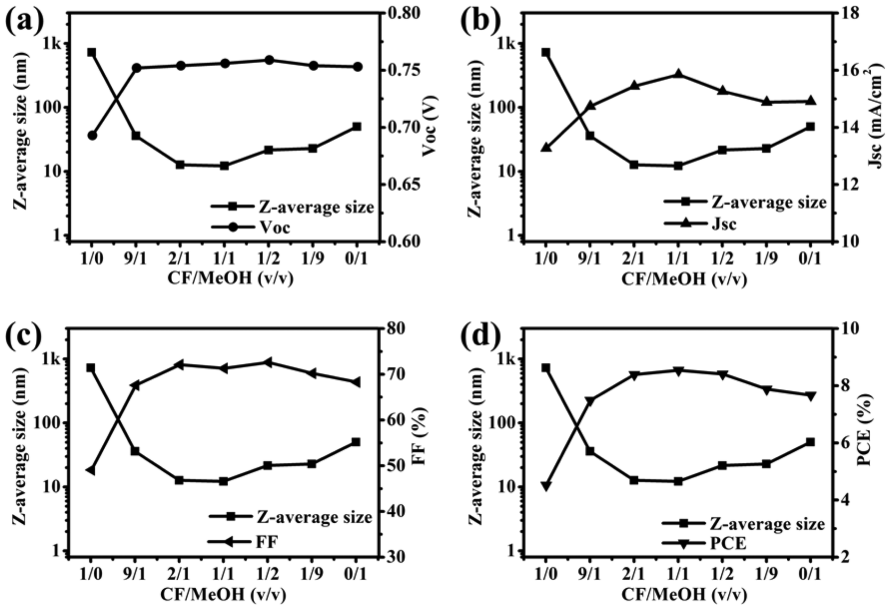

Figure 6. *Z*-Average size of ZnO NPs and photovoltaic parameters (a) V_{oc}, (b) J_{sc}, (c) FF, and (d) PCE of the devices as a function of different CF/MeOH ratios.

consistent with morphology differences revealed from the SEM images.

Through comparative analysis between the aggregation variation of ZnO NPs and the RMS roughness variation of ZnO nanofilm (Figures 3 and 5a–g), it is clear that the quality of ZnO nanofilm is dependent on the particle-size distributions of ZnO NPs. As shown in Figure 5h, the particle-size variation tendency to solvent ratios is similar to the roughness variation tendency. In other words, the ZnO NPs solution with high aggregation degree has numerous large clusters, which lead to incomplete coating on the ITO electrode and eventually form an uncontinuous film. The decrement of ZnO NPs aggregation indicates good ZnO NPs dispersion with narrow particle-size distribution, which results in the smooth and dense nanofilm. Therefore, we conclude that the morphology of ZnO nanofilm can be controlled by tuning CF/MeOH volume ratios.

The influences of the morphology of the ZnO buffer layer on the performance of inverted OSCs has been extensively studied.[49,50] The preferable morphology of the ZnO buffer layer is favorable for photovoltaic devices. Moreover, the above discussions of the size distributions effect on morphology of ZnO nanofilm are taken into consideration. So, the relationship between the particle-size distributions and the device parameters of inverted OSCs can be figured out, and the results are shown in Figure 6. When the volume ratio changed from pure CF to 9:1, V_{oc} is improved from 0.693 to 0.752 V. The *Z*-average size of ZnO NPs is sharply reduced with the MeOH increasing. The morphology of ZnO nanofilm is substantially improved shown in the SEM and AFM images.[51,52] And then V_{oc} keeps similar values with further changes of solvent ratios, which indicates that the V_{oc} value is insensitive to the morphology variation of the ZnO nanofilm. As observed from Figure 6b,c, the variations of J_{sc} and FF are negatively correlated with the *Z*-average size variation. Meanwhile, the surface morphology of the ZnO nanofilm is improved, which results in lower leakage current and a superior rectification ratio (see Figure 2b and Table 1). Therefore, J_{sc} and FF correspondingly increase in inverted OSCs.[53] With the increase of *Z*-average size, the J_{sc} and the FF are reduced. The results demonstrate that the particle size distributions strongly influence the J_{sc} and FF of the device by changing morphology of ZnO buffer layer. The PCE variation tendency is also opposite to the *Z*-average size variation, as observed in Figure 6d. And the best PCE (8.54%) is obtained in the lowest *Z*-average size when optimized solvent ratio (1:1) is applied. To summarize, the preferable particle size distributions is beneficial for the surface morphology of buffer layer as well as device performance.

To further analyze the effect of ZnO NPs aggregation on device performance, the maximum exciton generation rate (G_{max}) and exciton dissociation probability (P) for ZnO buffer layers based devices has been investigated. Figure 7 depicts the photocurrent density (J_{ph}) in a double-logarithmic plot as a function of effective applied voltage $V_{eff} = V_0 - V$, where V is the applied voltage and V_0 is the compensation voltage (determined at which $J_{ph} = 0$). The J_{ph} is obtained by the equation $J_{ph} = J_L - J_D$, J_L and J_D are the current densities under illumination and in dark condition, respectively. With the enhancement of V_{eff}, the J_{ph} increases sharply in the lower V_{eff}

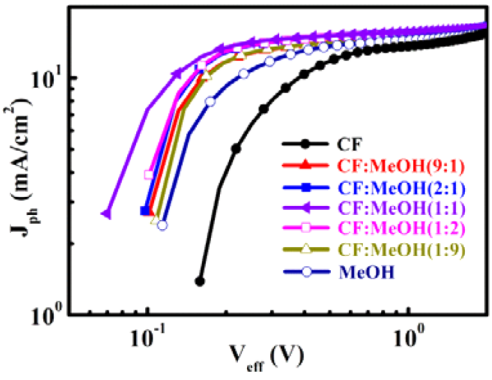

Figure 7. Plots of photocurrent density (J_{ph}) with respect to effective applied voltage (V_{eff}) for the devices based on ZnO buffer layers deposited from the ZnO NPs solution with different ratios.

dx.doi.org/10.1021/am5051789 | ACS Appl. Mater. Interfaces 2014, 6, 18172–18179

range and gradually saturates in the higher V_{eff} range.[54,55] Meanwhile, the saturation photocurrent (J_{sat}) in the devices are reached earlier when the dispersity of ZnO NPs solution is getting better. In general, the J_{sat} correlates with the value of G_{max}, which is mainly governed by light absorption and is given by $J_{sat} = qG_{max}L$, where q is the electronic charge and L is the thickness of active layer (110 nm).[56,57] As a result, the values of J_{sat} (i.e., V_{eff} = 1.5 V) and corresponding G_{max} for the devices are shown in Table S1 (Supporting Information). The G_{max} changes with solvents volume ratios of ZnO solution, which suggests that the morphology of the ZnO buffer layer influences the exciton generation rate. So, the superior ZnO nanofilm results in the maximum values of G_{max} (10.01×10^{27} m^{-3} s^{-1}, J_{sat} = 160 $A{\cdot}m^{-2}$). In addition, Figure S3 (Supporting Information) shows the normalized photocurrent (J_{ph}/J_{sat}). Under the short-circuit condition, the P values obtained from the ratio of J_{ph}/J_{sat} are improved by reducing ZnO NPs aggregation, which will decrease the exciton recombination rate. Consequently, the enhanced values in maximum exciton generation rate and exciton dissociation lead to the improvement of the device performance.[58]

4. CONCLUSION

In conclusion, a new and simple method to obtain a high quality ZnO buffer layer has been exploited. With adjusting solvent volume ratios of ZnO solution, the aggregations of ZnO NPs are controllably tuned and the superior dispersity of ZnO NPs is obtained (CF:MeOH = 1:1, v/v). This clearly exhibits the relationship between nanoparticles aggregation and solvent volume ratios. Similar change tendency of surface morphology of ZnO nanofilms have been shown. Due to the same reason, the exciton generation rate (G_{max}) and the exciton dissociation probability (P) of ZnO buffer layers are enhanced in photovoltaic device when the optimized solvents ratio is applied to disperse the ZnO nanoparticles. Therefore, the optimized ZnO dispersion results in the reduction of aggregation of ZnO NPs, which supports the morphology improvement of ZnO buffer layer. The device performance will be optimized consequently. The results put forward a facile method for the interfacial modification engineering in the fabrication of high-performance inverted OSCs.

■ ASSOCIATED CONTENT

Supporting Information

Device parameter distribution maps, photographs of ZnO NPs solutions with different solvents ratios, the corresponding plots of J_{ph}/J_{sat} with respect to effective applied voltage (V_{eff}) and the summary of J_{sat}, G_{max}, and P of PTB7:$PC_{71}BM$ devices using buffer layers deposited from the ZnO NPs solutions with different solvents ratios. This material is available free of charge via the Internet at http://pubs.acs.org.

■ AUTHOR INFORMATION

Corresponding Authors

*T. Jiu. E-mail: jiutonggang@nimte.ac.cn.
*J. Fang. E-mail: fangjf@nimte.ac.cn.

Notes

The authors declare no competing financial interest.

■ ACKNOWLEDGMENTS

The authors gratefully acknowledge the support of the National Natural Science Foundation of China (Nos. 51202264 and 51273208), and the Specialized Research Fund for the Spring Buds Talent Program (No. Y20804RA02). The work was also supported by Zhejiang Provincial and Ningbo City Natural Science Foundation of China (Nos. LR14E030002 and 2014A610037); the Starting Research Fund of Team Talent (Y10801RA01) in NIMTE.

■ REFERENCES

(1) Pagliaro, M.; Ciriminna, R.; Palmisano, G. Flexible Solar Cells. *ChemSusChem* **2008**, *1*, 880−891.
(2) Krebs, F. C.; Jørgensen, M.; Norrman, K.; Hagemann, O.; Alstrup, J.; Nielsen, T. D.; Fyenbo, J.; Larsen, K.; Kristensen, J. A Complete Process for Production of Flexible Large Area Polymer Solar Cells Entirely Using Screen Printing-First Public Demonstration. *Sol. Energy Mater. Sol. Cells* **2009**, *93*, 422−441.
(3) Brabec, C. J.; Sariciftci, N. S.; Hummelen, J. C. Plastic Solar Cells. *Adv. Funct. Mater.* **2001**, *11*, 15−26.
(4) Zhang, M.; Gu, Y.; Guo, X.; Liu, F.; Zhang, S.; Huo, L.; Russell, T. P.; Hou, J. Efficient Polymer Solar Cells Based on Benzothiadiazole and Alkylphenyl Substituted Benzodithiophene with a Power Conversion Efficiency Over 8%. *Adv. Mater.* **2013**, *25*, 4944−4949.
(5) Huo, L.; Zhang, S.; Guo, X.; Xu, F.; Li, Y.; Hou, J. Replacing Alkoxy Groups with Alkylthienyl Groups: A Feasible Approach to Improve the Properties of Photovoltaic Polymers. *Angew. Chem., Int. Ed.* **2011**, *50*, 9697−9702.
(6) You, J.; Dou, L.; Yoshimura, K.; Kato, T.; Ohya, K.; Moriarty, T.; Emery, K.; Chen, C. C.; Gao, J.; Li, G.; Yang, Y. A Polymer Tandem Solar Cell with 10.6% Power Conversion Efficiency. *Nat. Commun.* **2013**, *4*, 1446.
(7) bin Mohd Yusoff, A. R.; Lee, S. J.; Kim, H. P.; Shneider, F. K.; da Silva, W. J.; Jang, J. 8.91% Power Conversion Efficiency for Polymer Tandem Solar Cells. *Adv. Funct. Mater.* **2014**, *24*, 2240−2247.
(8) Zhang, W.; Wu, Y.; Bao, Q.; Gao, F.; Fang, J. Morphological Control for Highly Efficient Inverted Polymer Solar Cells via the Backbone Design of Cathode Interlayer Materials. *Adv. Energy Mater.* **2014**, DOI: 10.1002/aenm.201400359.
(9) de Jong, M. P.; van Ijzendoorn, L. J.; de Voigt, M. J. A. Stability of the Interface Between Indium-Tin-Oxide and Poly(3,4-ethylenedioxythiophene)/Poly(styrenesulfonate) in Polymer Light-Emitting Diodes. *Appl. Phys. Lett.* **2000**, *77*, 2255.
(10) Wong, K. W.; Yip, H. L.; Luo, Y.; Wong, K. Y.; Lau, W. M.; Low, K. H.; Chow, H. F.; Gao, Z. Q.; Yeung, W. L.; Chang, C. C. Blocking Reactions Between Indium-Tin Oxide and Poly(3,4-ethylene dioxythiophene):Poly(styrene sulphonate) with a Self-Assembly Monolayer. *Appl. Phys. Lett.* **2002**, *80*, 2788.
(11) Kawano, K.; Pacios, R.; Poplavskyy, D.; Nelson, J.; Bradley, D. D. C.; Durrant, J. R. Degradation of Organic Solar Cells Due to Air Exposure. *Sol. Energy Mater. Sol. Cells* **2006**, *90*, 3520−3530.
(12) Jørgensen, M.; Norrman, K.; Krebs, F. C. Stability/Degradation of Polymer Solar Cells. *Sol. Energy Mater. Sol. Cells* **2008**, *92*, 686−714.
(13) White, M. S.; Olson, D. C.; Shaheen, S. E.; Kopidakis, N.; Ginley, D. S. Inverted Bulk-Heterojunction Organic Photovoltaic Device Using a Solution-Derived ZnO Underlayer. *Appl. Phys. Lett.* **2006**, *89*, 143517.
(14) Waldauf, C.; Morana, M.; Denk, P.; Schilinsky, P.; Coakley, K.; Choulis, S. A.; Brabec, C. J. Highly Efficient Inverted Organic Photovoltaics Using Solution based Titanium Oxide as Electron Selective Contact. *Appl. Phys. Lett.* **2006**, *89*, 233517.
(15) Steim, R.; Choulis, S. A.; Schilinsky, P.; Brabec, C. J. Interface Modification for Highly Efficient Organic Photovoltaics. *Appl. Phys. Lett.* **2008**, *92*, 093303.
(16) Hau, S. K.; Yip, H.-L.; Ma, H.; Jen, A. K.-Y. High Performance Ambient Processed Inverted Polymer Solar Cells Through Interfacial Modification with a Fullerene Self-Assembled Monolayer. *Appl. Phys. Lett.* **2008**, *93*, 233304.
(17) Shin, K.-S.; Lee, K.-H.; Lee, H. H.; Choi, D.; Kim, S.-W. Enhanced Power Conversion Efficiency of Inverted Organic Solar

Cells with a Ga-Doped ZnO Nanostructured Thin Film Prepared Using Aqueous Solution. *J. Phys. Chem. C* **2010**, *114*, 15782−15785.
(18) Lee, H. J.; Hwang, J. H.; Choi, K. B.; Jung, S.-G.; Kim, K. N.; Shim, Y. S.; Park, C. H.; Park, Y. W.; Ju, B.-K. Effective Indium-Doped Zinc Oxide Buffer Layer on Silver Nanowires for Electrically Highly Stable, Flexible, Transparent, and Conductive Composite Electrodes. *ACS Appl. Mater. Interfaces* **2013**, *5*, 10397−10403.
(19) Stubhan, T.; Litzov, I.; Li, N.; Salinas, M.; Steidl, M.; Sauer, G.; Forberich, K.; Matt, G. J.; Halik, M.; Brabec, C. J. Overcoming Interface Losses in Organic Solar Cells by Applying Low Temperature, Solution Processed Aluminum-Doped Zinc Oxide Electron Extraction Layers. *J. Mater. Chem. A* **2013**, *1*, 6004−6009.
(20) Kyaw, A. K.; Wang, D. H.; Gupta, V.; Zhang, J.; Chand, S.; Bazan, G. C.; Heeger, A. J. Efficient Solution-Processed Small-Molecule Solar Cells with Inverted Structure. *Adv. Mater.* **2013**, *25*, 2397−2402.
(21) Chang, Y.-M.; Leu, C.-Y. Conjugated Polyelectrolyte and Zinc Oxide Stacked Structure as an Interlayer in Highly Efficient and Stable Organic Photovoltaic Cells. *J. Mater. Chem. A* **2013**, *1*, 6446−6451.
(22) Jo, S. B.; Lee, J. H.; Sim, M.; Kim, M.; Park, J. H.; Choi, Y. S.; Kim, Y.; Ihn, S. G.; Cho, K. High Performance Organic Photovoltaic Cells Using Polymer-Hybridized ZnO Nanocrystals as a Cathode Interlayer. *Adv. Energy Mater.* **2011**, *1*, 690−698.
(23) Small, C. E.; Chen, S.; Subbiah, J.; Amb, C. M.; Tsang, S.-W.; Lai, T.-H.; Reynolds, J. R.; So, F. High-Efficiency Inverted Dithienogermole-Thienopyrrolodione-based Polymer Solar Cells. *Nat. Photonics* **2012**, *6*, 115−120.
(24) Hu, T.; Li, F.; Yuan, K.; Chen, Y. Efficiency and Air-Stability Improvement of Flexible Inverted Polymer Solar Cells Using ZnO/Poly(ethylene glycol) Hybrids as Cathode Buffer Layers. *ACS Appl. Mater. Interfaces* **2013**, *5*, 5763−5770.
(25) Liao, S.-H.; Jhuo, H.-J.; Cheng, Y.-S.; Chen, S.-A. Fullerene Derivative-Doped Zinc Oxide Nanofilm as the Cathode of Inverted Polymer Solar Cells with Low-Bandgap Polymer (PTB7-Th) for High Performance. *Adv. Mater.* **2013**, *25*, 4766−4771.
(26) Wu, Y.; Zhang, W.; Li, X.; Min, C.; Jiu, T.; Zhu, Y.; Dai, N.; Fang, J. Solution-Processed Nanaybrid Cathode Interlayer for Inverted Organic Solar Cells. *ACS Appl. Mater. Interfaces* **2013**, *5*, 10428−10432.
(27) Sun, C.; Wu, Y.; Zhang, W.; Jiang, N.; Jiu, T.; Fang, J. Improving Efficiency by Hybrid TiO_2 Nanorods with 1,10-phenanthroline as a Cathode Buffer Layer for Inverted Organic Solar Cells. *ACS Appl. Mater. Interfaces* **2014**, *6*, 739−744.
(28) Liu, H.; Xu, J.; Li, Y.; Li, Y. Aggregate Nanostructures of Organic Molecular Materials. *Acc. Chem. Res.* **2010**, *43*, 1496−1508.
(29) Liu, H.; Zuo, Z.; Guo, Y.; Li, Y.; Li, Y. Supramolecular Interactions at the Inorganic-Organic Interface in Hybrid Nanomaterials. *Angew. Chem., Int. Ed.* **2010**, *49*, 2705−2707.
(30) Liu, H.; Wang, K.; Zhang, L.; Qian, X.; Li, Y.; Li, Y. Selectively Recognizing Organic Semiconducting Molecules on Solid State Molecular Cages Based on ZnOTCPP. *Dalton Trans.* **2014**, *43*, 432−438.
(31) Li, P.; Sun, C.; Jiu, T.; Wang, G.; Li, J.; Li, X.; Fang, J. High-Performance Inverted Solar Cells Based on Blend Films of ZnO Naoparticles and TiO_2 Nanorods as a Cathode Buffer Layer. *ACS Appl. Mater. Interfaces* **2014**, *6*, 4074−4080.
(32) Chang, J.; Lin, Z.; Zhu, C.; Chi, C.; Zhang, J.; Wu, J. Solution-Processed LiF-Doped ZnO Films for High Performance Low Temperature Field Effect Transistors and Inverted Solar Cells. *ACS Appl. Mater. Interfaces* **2013**, *5*, 6687−6693.
(33) Niedermeier, M. A.; Tainter, G.; Weiler, B.; Lugli, P.; Müller-Buschbaum, P. Fabrication of Hierarchically Structured Titania Thin Films via Combining Nano-Imprint Lithography with Block Copolymer Assisted Sol−Gel Templating. *J. Mater. Chem. A* **2013**, *1*, 7870−7873.
(34) Niedermeier, M. A.; Groß, I.; Müller-Buschbaum, P. Structuring of Titania Thin Films on Different Length Scales via Combining Block Copolymer Assisted Sol−Gel Templating with Wet-Imprinting. *J. Mater. Chem. A* **2013**, *1*, 13399−13403.
(35) Crossland, E. J. W.; Kamperman, M.; Nedelcu, M.; Ducati, C.; Wiesner, U.; Smilgies, D.-M.; Toombes, G. E. S.; Hillmyer, M. A.; Ludwigs, S.; Steiner, U.; Snaith, H. J. A Bicontinuous Double Gyroid Hybrid Solar Cell. *Nano Lett.* **2009**, *9*, 2807−2812.
(36) Suresh, V.; Huang, M. S.; Srinivasan, M. P.; Krishnamoorthy, S. In Situ Synthesis of High Density Sub-50 nm ZnO Nanopatterned Arrays Using Diblock Copolymer Templates. *ACS Appl. Mater. Interfaces* **2013**, *5*, 5727−5732.
(37) Kwong, C. Y.; Djurišić, A. B.; Chui, P. C.; Cheng, K. W.; Chan, W. K. Influence of Solvent on Film Morphology and Device Performance of Poly(3-hexylthiophene):TiO_2 Nanocomposite Solar Cells. *Chem. Phys. Lett.* **2004**, *384*, 372−375.
(38) Chen, L.-M.; Hong, Z.; Li, G.; Yang, Y. Recent Progress in Polymer Solar Cells: Manipulation of Polymer:Fullerene Morphology and the Formation of Efficient Inverted Polymer Solar Cells. *Adv. Mater.* **2009**, *21*, 1434−1449.
(39) Su, M. S.; Kuo, C. Y.; Yuan, M. C.; Jeng, U. S.; Su, C. J.; Wei, K. H. Improving Device Efficiency of Polymer/Fullerene Bulk Heterojunction Solar Cells through Enhanced Crystallinity and Reduced Grain Boundaries Induced by Solvent Additives. *Adv. Mater.* **2011**, *23*, 3315−3319.
(40) Pacholski, C.; Kornowski, A.; Weller, H. Self-Assembly of ZnO: From Nanodots to Nanorods. *Angew. Chem., Int. Ed.* **2002**, *41*, 1188−1191.
(41) Beek, W. J. E.; Wienk, M. M.; Kemerink, M.; Yang, X.; Janssen, R. A. J. Hybrid Zinc Oxide Conjugated Polymer Bulk Heterojunction Solar Cells. *J. Phys. Chem. B* **2005**, *109*, 9505−9516.
(42) Li, P.; Li, X.; Sun, C.; Wang, G.; Li, J.; Jiu, T.; Fang, J. Performance Enhancement of Inverted Polymer Solar Cells with Fullerene Ester Derivant-Modified ZnO Film as Cathode Buffer Layer. *Sol. Energy Mater. Sol. Cells* **2014**, *126*, 36−41.
(43) He, Z.; Zhong, C.; Su, S.; Xu, M.; Wu, H.; Cao, Y. Enhanced Power-Conversion Efficiency in Polymer Solar Cells Using an Inverted Device Structure. *Nat. Photonics* **2012**, *190*, 591−595.
(44) Tao, C.; Ruan, S.; Zhang, X.; Xie, G.; Shen, L.; Kong, X.; Dong, W.; Liu, C.; Chen, W. Performance Improvement of Inverted Polymer Solar Cells with Different Top Electrodes by Introducing a MoO_3 Buffer Layer. *Appl. Phys. Lett.* **2008**, *93*, 193307.
(45) You, J.; Chen, C. C.; Dou, L.; Murase, S.; Duan, H. S.; Hawks, S. A.; Xu, T.; Son, H. J.; Yu, L.; Li, G.; Yang, Y. Metal Oxide Nanoparticles as an Electron-Transport Layer in High-Performance and Stable Inverted Polymer Solar Cells. *Adv. Mater.* **2012**, *24*, 5267−5272.
(46) Greiner, M. T.; Lu, Z.-H.; Helander, M. G.; Tang, W.-M.; Wang, Z.-B.; Qiu, J.; Lu, Z.-H. Universal Energy-Level Alignment of Molecules on Metal Oxides. *Nat. Mater.* **2012**, *11*, 76−81.
(47) Segets, D.; Gradl, J.; Taylor, R. K.; Vassilev, V.; Peukert, W. Analysis of Optical Absorbance Spectra for the Determination of ZnO Nanoparticle Size Distribution, Solubility, and Surface Energy. *ACS Nano* **2009**, *3*, 1703−1710.
(48) Choi, K.-C.; Lee, E.-J.; Baek, Y.-K.; Kim, M.-J.; Kim, Y.-D.; Shin, P.-W.; Kim, Y.-K. Modifying Hydrogen Bonding Interaction in Solvent and Dispersion of ZnO Nanoparticles: Impact on the Photovoltaic Performance of Inverted Organic Solar Cells. *RSC Adv.* **2014**, *4*, 7160−7166.
(49) Ma, Z.; Tang, Z.; Wang, E.; Andersson, M. R.; Inganas, O.; Zhang, F. Influences of Surface Roughness of ZnO Electron Transport Layer on the Photovoltaic Performance of Organic Inverted Solar Cells. *J. Phys. Chem. C* **2012**, *116*, 24462−24468.
(50) Liang, Z.; Zhang, Q.; Wiranwetchayan, O.; Xi, J.; Yang, Z.; Park, K.; Li, C.; Cao, G. Effects of the Morphology of a ZnO Buffer Layer on the Photovoltaic Performance of Inverted Polymer Solar Cells. *Adv. Funct. Mater.* **2012**, *22*, 2194−2201.
(51) He, C.; Zhong, C.; Wu, H.; Yang, R.; Yang, W.; Huang, F.; Bazan, G. C.; Cao, Y. Origin of the Enhanced Open-Circuit Voltage in Polymer Solar Cells via Interfacial Modification Using Conjugated Polyelectrolytes. *J. Mater. Chem.* **2010**, *20*, 2617−2622.
(52) Mihailetchi, V. D.; Blom, P. W. M.; Hummelen, J. C.; Rispens, M. T. Cathode Dependence of the Open-Circuit Voltage of

Polymer:Fullerene Bulk Heterojunction Solar Cells. *J. Appl. Phys.* **2003**, *94*, 6849−6854.
(53) Shao, S.; Zheng, K.; Pullerits, T.; Zhang, F. Enhanced Performance of Inverted Polymer Solar Cells by Using Poly(ethylene oxide)-Modified ZnO as an Electron Transport Layer. *ACS Appl. Mater. Interfaces* **2013**, *5*, 380−385.
(54) Mihailetchi, V.; Wildeman, J.; Blom, P. Space-Charge Limited Photocurrent. *Phys. Rev. Lett.* **2005**, *94*, 126602.
(55) Mihailetchi, V. D.; Xie, H.; de Boer, B.; Koster, L. A.; Blom, P. W. Charge Transport and Photocurrent Generation in Poly(3-hexylthiophene):Methanofullerene Bulk-heterojunction Solar Cells. *Adv. Funct. Mater.* **2006**, *16*, 699−708.
(56) Chen, F.-C.; Wu, J.-L.; Lee, C.-L.; Hong, Y.; Kuo, C.-H.; Huang, M. H. Plasmonic-Enhanced Polymer Photovoltaic Devices Incorporating Solution-Processable Metal Nanoparticles. *Appl. Phys. Lett.* **2009**, *95*, 013305.
(57) Xu, M.-F.; Zhu, X.-Z.; Shi, X.-B.; Liang, J.; Jin, Y.; Wang, Z.-K.; Liao, L.-S. Plasmon Resonance Enhanced Optical Absorption in Inverted Polymer/Fullerene Solar Cells with Metal Nanoparticle-Doped Solution-Processable TiO_2 Layer. *ACS Appl. Mater. Interfaces* **2013**, *5*, 2935−2942.
(58) He, Z.; Zhong, C.; Huang, X.; Wong, W.-Y.; Wu, H.; Chen, L.; Su, S.; Cao, Y. Simultaneous Enhancement of Open-Circuit Voltage, Short-Circuit Current Density, and Fill Factor in Polymer Solar Cells. *Adv. Mater.* **2011**, *23*, 4636−4643.